Altimetric Ku-band Radar Observations of Snow on Sea Ice Simulated with SMRT

Julien Meloche[1], Melody Sandells[2], Henning Löwe[3], Nick Rutter[2], Richard Essery[4], Ghislain Picard[5], Randall K. Scharien[6], Alexandre Langlois[7], Matthias Jaggi[3], Josh King[1,†], Peter Toose[1], Jérôme Bouffard[8], Alessandro Di Bella[8], and Michele Scagliola[8]

[1]Climate Research Division, Environment Climate Change Canada, Toronto, Canada
[2]Department of Geography and Environmental Sciences, Northumbria University, Newcastle-Upon-Tyne, UK
[3]WSL Institute for Snow and Avalanche Research SLF, Davos, Switzerland
[4]Department of Geosciences, University of Edinburgh, Edinburgh, UK
[5]Univ. Grenoble Alpes, CNRS, IGE, 38000 Grenoble, France
[6]Department of Geography, University of Victoria, Victoria, Canada
[7]Département de géomatique appliquée, Université de Sherbrooke, Sherbrooke, Canada
[8]ESA-ESRIN, Frascati, Italy
[†]deceased, 21 February, 2023

Correspondence: Julien Meloche (julien.meloche@ec.gc.ca)

Abstract. Sea ice thickness is essential for climate studies and numerical weather prediction. Radar altimetry has provided sea ice thickness measurement since the launch of ERS-1 and currently through CryoSat-2, Sentinel-3 and Altika but uncertainty in the scattering horizon used to retrieve sea ice thickness arises from interactions between the emitted signal and snow cover on the ice surface. Therefore, modelling the scattering of the electromagnetic waves with the snowpack and ice is necessary to retrieve the sea ice thickness accurately. The Snow Microwave Radiative Transfer (SMRT) model was used to simulate the low resolution altimeter waveform echo from the snow-covered sea ice, using in-situ measurements as input. Measurement from four field campaigns were used: Cambridge Bay, Eureka Sound and near Alert, Nunavut, Canada in April 2022 in the cold and later winter condition when snow and ice thickness are neat their seasonal maxima prior to melt. In-situ measurements included snow temperature, salinity, density, specific surface area, microstructure from X-ray tomography and surface roughness measurements using structure from motion photogrammetry. Evaluation of SMRT in altimeter mode was performed against CryoSat-2 waveform data in pseudo-low-resolution mode. Simulated and observed waveforms showed good agreement, although it was necessary to adjust sea ice roughness. The retrieved roughness (root-mean-square height) in Cambridge Bay was 2.1 mm and 1.6 mm in Eureka, which was close to the observed value of 1.4 mm for flat sea ice. In addition, simulations of backscatter in preparation for the European Space Agency's CRISTAL mission demonstrated the dominance of scattering from the snow surface at Ku and Ka-band. However, these findings depend on the parameterisation of the roughness. The scattering from the snow surface dominates when roughness is high, but the interface return dominates if the roughness is low (< 2.5 mm). This is the first study to consider scattering within the snow and demonstrate the origin of CryoSat-2 signals. This work paved the way to a new physical retracker using SMRT to retrieve snow depth and sea ice thickness for radar altimeter missions.

1 Introduction

Sea ice and snow in polar environments are key components in Earth surface energy balance for climate prediction. The strong albedo from snow on sea ice reflects most of the solar energy and keeps the ocean from warming. The reduction of sea ice due to a warmer climate (Derksen et al., 2019; Richter-Menge et al., 2017) modifies the surface energy balance and creates positive feedback on surface temperature (Goosse et al., 2018; Serreze and Barry, 2011). Monitoring of cryospheric parameters such as sea ice and snow thickness on large scale is therefore key in a changing climate. Sea ice thickness data can also be assimilated in meteorological models to perform seasonal forecasts of sea ice extent (Blockley and Peterson, 2018; Allard et al., 2018). Radar altimetry is a useful tool to monitor sea ice thickness over polar environments by measuring the ice freeboard. However, snow properties such as thickness and density are necessary to infer total sea ice thickness for this measurement, through the buoyancy principle and assuming hydrostatic equilibrium (Ricker et al., 2014). Moreover, surface properties like roughness, salinity, density, temperature and microstructure of the snow and sea ice affect the accuracy of the retrieval by modifying the measured waveform of the radar (Nandan et al., 2020; Landy et al., 2020).

Radar altimeters measure surface elevations using the two-way travel time of the emitted waves, and reflected from the surface. A waveform (measurement of returned power over time) is used to analyse the reflected signal from the surface that comes from multiple facets within the sensor footprint. The range to the surface is represented by the mean return of the facets at nadir as the tracking point (Quartly et al., 2019). The tracking point is defined on the leading edge portion (rise in power) of the waveform based on different thresholds, usually from 50 to 95% depending on the surface properties. Multiple corrections need to be applied from atmospheric, tidal and sensor effects (Ricker et al., 2016) in order to correctly estimate the range with the tracking point. This process is referred to waveform "retracking" with either an empirical or physical bases. Empirical retrackers are more computationally efficient and are solely based on getting a robust estimate of the range compared to methods that are based on mathematical models of the physical interaction between the transmitted pulse and the scattering surface (Quartly et al., 2019). Empirical retrackers are favoured with the first generation of pulse-limited altimeter (low resolution). Products from the new generation of Synthetic Aperture Radar (SAR) altimeters like CryoSat-2 utilize physical models (Dinardo et al., 2018) to model SAR waveform and more complex surfaces including Multi-Year Ice (MYI), First Year Ice (FYI) and leads.

One of the mathematical model of pulse-limited altimeter behaviour is given in Brown (1977). The Brown (1977) model works well for surface-dominated reflected echos such as on the ocean and land ice (Hayne, 1980; Ferraro and Swift, 1995). This formulation is not typically used for sea ice because it cannot model adequately specular reflection from leads (Landy et al., 2019) or smooth FYI. FYI can have a steeper trailing edge decay and different Pulse Peakiness (PP) which can be used to discriminate with MYI (Fredensborg Hansen et al., 2021). This is partly due to FYI being newly formed ice and smoother than older MYI or deformed FYI and therefore has waveform characteristics that correspond to a specular reflection like leads (open flat ocean) with higher PP and faster decay.

Physical retrackers are based on electromagnetic theory to model the interaction of radar signals with the surface (Wingham et al., 2004). Backscattering contribution from the surface (snow and ice) affects the waveform and therefore the retrieval of the ice thickness. Kwok (2014) simulated a height correction factor as a function of snow depth using a single layer of snow with

a rough snow-sea ice interface. Nandan et al. (2017) and Nandan et al. (2020) added more complex snow properties and snow salinity to the correction factor. This was done by using a permittivity model for snow that accounts for dry/wetness, density and brine concentration. They all found that snow properties affects the detection of the ice surface by shifting the scattering horizon of the surface upwards from the snow-sea ice interface. Kurtz et al. (2014) simulated a full waveform of CryoSat-2 in SAR mode rather than the Brown (1977) pulse-limited altimeter (pseudo Low Resolution Mode - pLRM for CryoSat-2), and included leads as a separate surface type. Physical retrackers like the CryoSat-2 WaveForm Fitting method (CS2WfF) (Kurtz et al., 2014) and SAMOSA+ (Dinardo et al., 2018) have added a parameter to model peaky waveforms over specular surfaces. However, they neglected the effect of snow cover and assumed the reflection coming strictly from the snow-ice interface. Fons and Kurtz (2019) improved this model by adding a snow scattering layer for Antarctic sea ice thickness retrieval. Landy et al. (2019) provided the most complete model of both SAR and pLRM mode for sea ice by incorporating roughness at two scales (footprint and wavelength) with a multiple facet numerical approach and the Integral Equation Model (IEM) for surface scattering. They also added volume scattering of snow using the Mie scattering theory for spherical ice particles, neglecting the dense media effects (Tsang et al., 2007; Picard et al., 2022), and assumed a single grain size and no volume scattering from brine. The facet-based model lacks a complete representation of complex snow microstructure (Sandells et al., 2022) and solution of the radiative transfer equation. Our understanding of the effect of snow on sea ice on altimeter waveforms is still lacking.

Snow depth and density are key for ice thickness retrieval because they are used to calculate the ice thickness. Therefore it is important to retrieve snow depth as well as ice freeboard from satellite observations. Snow depth retrieval may be possible from the range difference at Ku and Ka-band (Guerreiro et al., 2016; Lawrence et al., 2018) under the assumption that the scattering horizons are located directly at the snow-ice interface in Ku band and at the air-snow in Ka band. However, as snow properties affect the Ku-band (Nandan et al., 2020; Landy et al., 2019) and Ka-band signal (Guerreiro et al., 2016; Larue et al., 2021), the assumption of scattering purely at these interfaces must be challenged. Investigating the scattering of Ku and Ka-band altimeter signals with a radiative transfer model that accounts for multiple layers, complex snow microstructure, wet snow, salinity, sea ice properties and rough interfaces is needed. The Snow Microwave Radiative Transfer (SMRT) model is a state-of-the-art radiative transfer model of multi-layered snow and ice at microwave frequencies (Picard et al., 2018) that allows such an investigation.

The Altimetric Ku-Band Radar Observations Simulated with SMRT (AKROSS) project was designed to provide the first evaluation of the SMRT model in altimeter mode for snow on sea ice. This model was extended to include a time-dependent radiative transfer solver for altimetry by Larue et al. (2021) and evaluated at S-, Ku- and Ka-band for ENVISAT, AltiKa and Sentinel-3A over the Antarctic Ice-Sheet. SMRT has been mostly evaluated over land (Vargel et al., 2020; Sandells et al., 2022), ice-sheets (Larue et al., 2021; Picard et al., 2022) and lake ice (Murfitt et al., 2022, 2023). Sea ice layers were added to SMRT in 2018 but evaluation of SMRT over sea ice has only been performed recently for passive microwave sensors Soriot et al. (2022). These authors used SMRT to classify snow on sea ice with passive and active microwave signatures and recently SMRT was evaluated with passive microwave observations over sea ice at L-band (Fan et al., 2023). Here, we present the first

study that provides SMRT forward model evaluation against satellite observations of snow on sea ice for altimetry using in-situ snow microstructure measurements as input.

The purpose of this paper is to evaluate SMRT for altimeter over sea ice by 1) Evaluating the overall fit of the waveform with observation of CryoSat-2, 2) Investigating the sensitivity of the Ku and Ka bands to snow and sea ice parameters in preparation for the launch of European Space Agency's future Copernicus Polar Ice and Snow Topography Altimeter (CRISTAL) mission. (Kern et al., 2020).

2 Methods

2.1 Study Site

Four different datasets were used for evaluation of SMRT in altimeter mode of snow on sea ice. The field sites are located in the Arctic Ocean and in the Canadian Arctic Archipelago, as shown in Figure 1. Ground campaigns in 2016 and 2017 were associated with CryoVex and Operation IceBridge airborne campaigns. Ground campaigns in 2022 (AKROSS) were associated with the AKROSS project and Environment and Climate Change Canada's evaluation of NASA's Ice, Cloud and land Elevation Satellite (ICESat-2) products in the Canadian Arctic. The sites observed in 2017, referred to as Alert-17 in this paper, are located in the Arctic Ocean north of Alert, Nunavut, Canada and are over MYI. Measurements made in 2016 and 2022 were located in Eureka Sound, and Cambridge Bay in the Canadian Arctic Archipelago, referred to Eureka-16, Eureka-22 and CB-22 in this paper. Eureka-16 was characterised by FYI conditons with some localized MYI floes (Figure 1). The Eureka-22 and CB-22 were only FYI conditions. Sentinel-1 images in Figure 1 highlight the varying backscatter from local ice conditions. Pulse limited footprint centre points of CryoSat-2 observations from the temporally closest overpass dates to the in situ measurements are also shown in Figure 1 by hollow red circles (1.6 km in diameter), with the location of in-situ observations either located within the CryoSat-2 footprint (CB-22), or located within 40 kilometers on similar sea ice types illustrated by blue (FYI) or purple (MYI) solid circles.

2.2 Data

The most recent campaigns, CB-22 and Eureka-22, produced a complete suite of in-situ field measurements, including roughness, salinity, temperature and micro-CT measurements of snow (micro-CT only in CB-22), allowing for a full evaluation of SMRT over sea ice. Table 1 1 provides a complete list of measured variables available for each campaign. The Alert-17 and Eureka-16 datasets are limited to the snow microstructural information from the SMP and do not have roughness. All sites have salinity and temperature measurements, which influence microwave scattering within snow (Nandan et al., 2017; Kwok, 2014).

For CB-22 and Eureka-22, measurements of snow density, temperature, salinity, specific surface area (SSA) and stratigraphy were made in vertical profiles in a snow pit for each site. For density and SSA, two vertical profiles of measurements were made in each snow pit, , following the protocols discussed and illustrated in (Tsang et al., 2022), Figure A1b. Snow samples
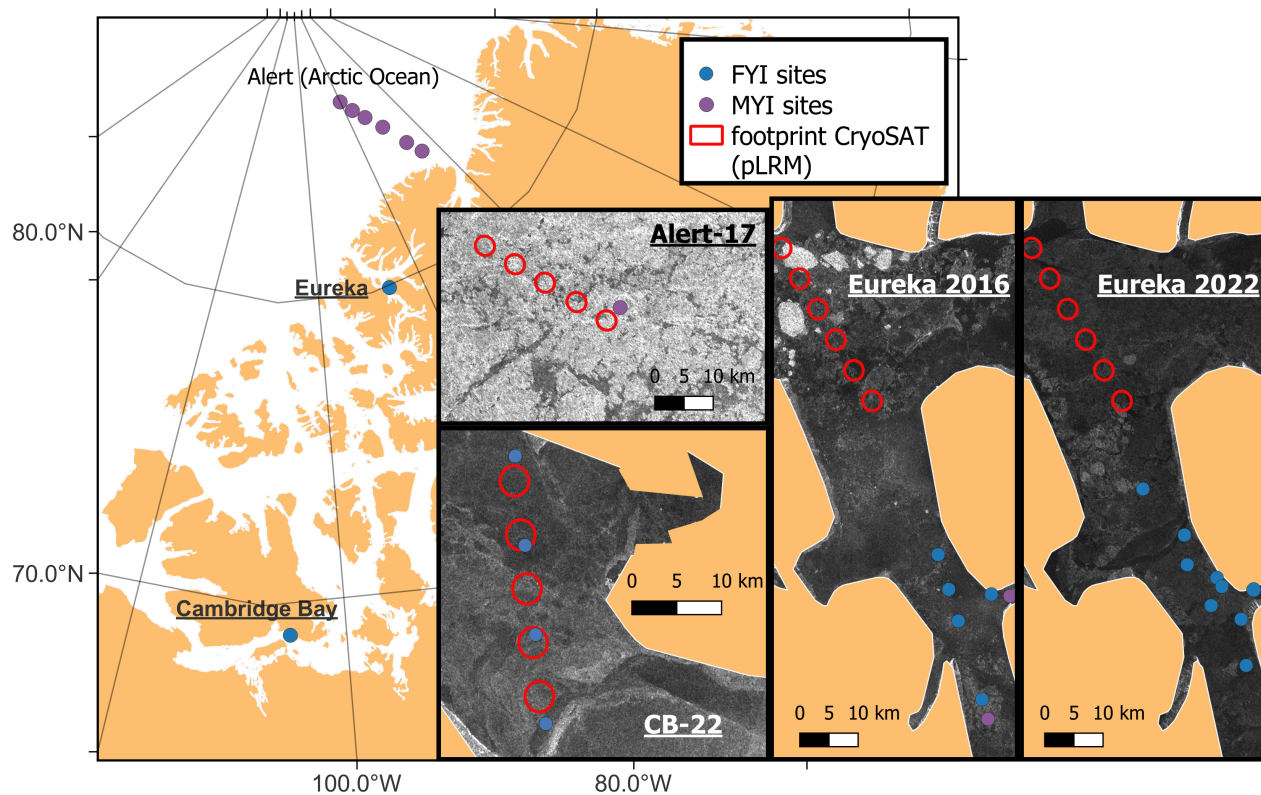
Figure 1. Location of Alert, Eureka, and Cambridge Bay (CB) evaluation field sites. Inset shows Sentinel-1 images in HH pol (CB: 2022-04-24, Alert: 2017-04-30, Eureka: 2016-04-15 and 2022-04-21) to show ice conditions at each site, bright regions correspond to MYI conditions. Locations of in-situ sites (FYI and MYI) and CryoSat-2 observations are shown.

from within the same vertical profile layer as the density and SSA measurements were bagged and labeled in the snowpit, and then brough back to the research facilities where they were melted and subsequently measured for salinity using the EcoSense

120 EC300A conductivity meter. Salinity was measured in melted samples of snow extracted from the same vertical positions in the profile as density measurements. In total, 809 SMP profiles were recorded on Arctic sea ice for all four field campaigns (Total snowpit coincident SMP sites: 20 in Eureka-16, 6 in Alert-17, 19 in Eureka-22, 4 in CB-22). In-addition to collecting SMP profiles at snowpit locations, transects around each snowpit with varying horizontal spacings were established to characterize variations in density, SSA and stratigraphy at spatial scales of up to 100 m following similar protocols as described in Tsang et

125 al., 2022 Appendix A, and illustrated in Figure A1b. An average of 69 SMP profiles were collected at each snow survey site in Eureka-16, 11 SMP profiles in Alert-17, 31 SMP profiles in CB-22 and 9 SMP profiles in Eureka-22. The Eureka-22 campaign

Measurement	Eureka-16	Alert-17	Eureka-22	CB-22
Snow pit stratigraphy	-	-	x	x
Magnaprobe depth	x	x	x	x
Snow cutter density profiles	x	x	x	x
Snow MicroPenetrometer (SMP)	x	x	x	x
Snow Integrating Sphere (SSA)	-	-	x	x
Micro-CT Microstructure	-	-	-	x
Snow temperature	x	x	x	x
Boundary roughness	-	-	x	x
Ice thickness (in-situ)	x	x	x	x
Ice / snow salinity	x	x	x	x
CryoSat-2 overpass	x	x	x	x

Table 1. Overview of available data for SMRT evaluation. x: data available, -: not observed. 2016 data reported in King et al. (2020), 2017 data reported in Haas et al. (2017).

did not follow the same SMP spatial sampling protocols as the other campaigns, and instead surveyed spatial variability in narrower transects along 10's of kilometers of ICESat-2 satellite ground tracks, measuring 5 SMP profiles coincident to 56 ice thickness measurements, spaced out every 500 to 2000 m apart.

130   All campaigns measured snow microstructure with a combination of x-ray tomography (micro-CT) only for CB-22 and SMP snow SSA for all sites. The vertical resolution of the SMP derived density and SSA depends on the window size used in the derivation of SMP coefficients, which was 5 mm in this case. The snow density (ρ) and SSA of the SMP were then calculated as:

$$\rho_{smp} = a_1 + a_2 \ln\left(\tilde{F}\right) + a_3 \ln\left(\tilde{F}\right) L + a_4 L \tag{1}$$

135    $$SSA_{smp} = \exp(b_1 + b_2 \ln\left(L\right) + b_3 \ln\left(\tilde{F}\right)) \tag{2}$$

where $\tilde{F}$ is the median of the penetration resistance force and L is the mean distance between structural elements in 3D space (Löwe and van Herwijnen, 2012). Coefficients are a_1 = 312.54, a_2 = 50.27, a_3 = -50.26 and a_4 = -88.15, from King et al. (2020) and b_1=2.37, b_2 =-0.7 and b_3 =-0.06 from Montpetit et al. (2024). Density coefficients from King et al. (2020) were used to derive the density profile. For SSA, as no independent SSA observations were made for Alert-17 or Eureka-16, Arctic SSA

140   coefficients were derived from the Montpetit et al. (2024) dataset over terrestrial snow in Trail Valley Creek, Inuvik, Canada following the methodology of King et al. (2020). Similarity between SMP density coefficients of the terrestrial and sea ice snow suggested that the transferability of SSA coefficients is a reasonable assumption.

From the SMP profiles, a rolling median over 3 cm was applied to produce layers of 3 cm for SMRT. For sensitivity tests, 1 cm and 5 cm rolling medians were also used in section 3.3. Layers in SMRT should not be much smaller than the wavelength of the signal (Picard et al., 2018), which is ≈ 2.2 cm for Ku-band and ≈ 0.8 cm for Ka-band assuming speed of light in air. Under these assumptions, main layers are captured, but high resolution features such as thin ice crusts may be missed. SMP measurements do not always capture the full profile as the penetration depth is manually set to sample less than the total snow depth to protect the sensitive tip from damage at the sea ice interface. Simulations capture the full depth of the profile by matching depth measured and the SMP depth with any additional depth attributed to and assumed to have the same density as the bottom snow layer. Figure 2 illustrates the range of density and SSA measured at the four sites. Snow was deepest at the Alert-17 MYI site and also had the lowest median SSA. Eureka-22 and CB-22 were the shallowest and most dense snow, with comparable SSA to Eureka-16.

During the CB-22 campaign, snow samples were drilled in the field following procedures from MOSAiC (Nicolaus et al., 2022) and transported from Cambridge Bay to Davos within 4 days in strict isothermal conditions at -21°C, to be scanned at the WSL Institute for Snow and Avalanche Research SLF. For the present work, only uncasted samples were used. Non-intact portions of the samples were identified after micro-CT scanning and discarded from the analysis. A CB-22 snowpack typically consists of 2 samples (height ≈ 10 cm) that was scanned and analyzed in moving window mode following standard means (Sandells et al., 2022). Density and microstructure model parameters for SMRT (Picard et al., 2018) were derived as profiles with vertical resolution of ≈ 0.8 cm that were used for the simulations presented in section 3.3. In total, four snow profiles (referred to as AK1-4 henceforth, representing the blue spots from North to South in Figure 1) were analyzed in this way. Figure 3 illustrates the varying ice volume fraction derived from three different snow measurement techniques with varying levels of vertical resolution: pit density cutter (3 cm), SMP rolling median window (5 cm and 1 cm) , and micro-CT observations (0.8 cm). Density cutter measurements showed the least variability in ice volume fraction($\phi = 0.4 \pm 0.03$), and micro-CT the greatest ($\phi = 0.37 \pm 0.06$). It is known that the volume fraction (snow density) measured by a CT is more accurate representation than other measurement method.

Measured small-scale roughness parameters were determined from in-situ photogrammetry recorded during the CB-22 and Eureka-22 campaigns, using the Structure from Motion (SfM) technique as described in Meloche et al. (2021). Once 3D point clouds were created for both snow and ice surface, roughness parameters could be calculated but the method deviated from Meloche et al. (2021) because the sites measured varied in area 2-4 m^2, compared to 0.5 m^2 for Meloche et al. (2021). Following a similar procedure from Landy et al. (2015a), the full area was detrended from curvature or large height deviation by sub sampling (n = 20) smaller areas of 0.2 m^2 (circle with r = 0.25) and applying the same measurement procedure of fitting a plane to this subset. Each subset will fit a different local plane. The height standard deviation was calculated with respect to the local plane of each subset. The correlation length was estimated using the autocorrelation function of heights. The mean for all subsets was used to estimate both roughness parameters. Two point clouds were created from in-situ photogrammetry at every sites for the snow surface and the sea ice surface. In total, 8 surfaces were used to derive roughness parameters for snow and 8 for sea ice surfaces.
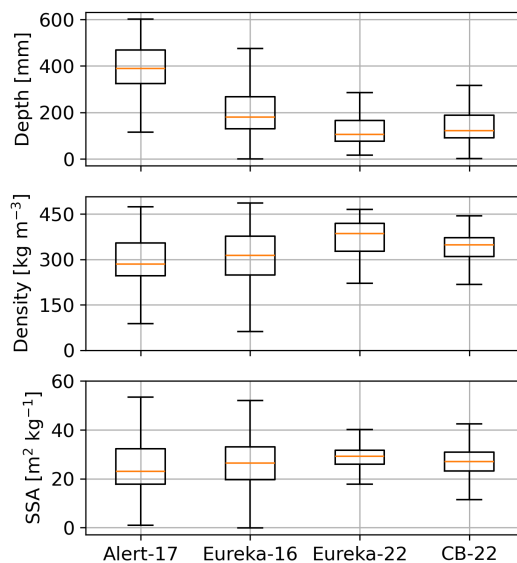
Figure 2. Box plot of SMP parameters derived from profile for Alert-17, Eureka (16 FYI only and 22) and CB-22. Density and SSA are derived from coefficients from King et al. (2020) and Montpetit et al. (2024).
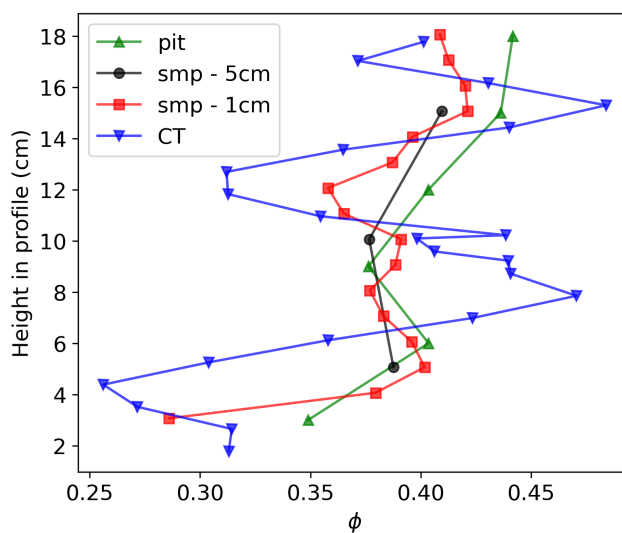
Figure 3. Comparison of volume fraction between snowpit measurements (density cutter), SMP and micro-CT measurements for CB-22.

2.3 Simulation Framework

2.3.1 Snow Microwave Radiative Transfer (SMRT) model

The SMRT model was adapted for altimeter applications by Larue et al. (2021). SMRT is a multilayer model, with each snow
layer represented by temperature, density, thickness and microstructure parameters. The layers are separated by interfaces,
which are flat (i.e. reflectivity is calculated with Fresnel equations) by default but rough interfaces may also be specified.
Beneath the snow, ice layers may be specified with different parameters; type (fresh, first year or multiyear sea ice), temperature,
density, thickness, microstructural parameters and salinity. First year sea ice is represented as brine scatterers within a pure ice
background whereas multiyear ice is represented as air bubble scatterers within a slightly saline ice background. The substrate
beneath the lowest layer can be represented in a variety of ways: by permittivity, reflectivity or empirical soil model. For the
simulations presented here, the substrate is water with a flat interface.

Input parameters are used with the permittivity model to calculate the electromagnetic properties i.e. scattering and absorption coefficients and phase functions. These parameters depend on which electromagnetic model is used (e.g. Improved Born
Approximation (IBA) or Dense Media Radiative Transfer model with Quasi-Crystalline approximation (DMRT-QCA)). The
electromagnetic parameters are then used with the interface boundary conditions to solve the radiative transfer equation. SMRT
was originally developed with a discrete ordinates radiative transfer solver (DORT), which enabled simulation of brightness
temperature for passive mode and backscatter for active mode (Picard et al., 2018). Extension of SMRT for altimeter applications uses the existing SMRT core infrastructure to construct the medium and calculate its electromagnetic properties.
However, simulation of the waveform is then performed via the new time-dependent radiative transfer solver outlined in Larue
et al. (2021) instead of DORT. Receiving antennae collect radiation over discrete intervals of time known as gates or bins.
Penetration of the signal into the snowpack is taken into account, as well as the delay implied by the horizontal extend of the
beam, but returns from elsewhere within the beamwidth at a particular time will be from shallower depths, as illustrated by the
blue grid in Figure 1b from Larue et al. (2021). These grids are combined to form a series of thinner layers in SMRT for the
purpose of the calculation. The width of the gate depends on the pulse bandwidth. For CryoSat-2 the pulse bandwidth is 320
MHz, which means the altimeter gate sampling rate Δt is 3.125 nanoseconds. For LRM waveforms (only waveforms currently
implemented in SMRT), the returned power is then calculated:

$$P_r(t) = pdf(t) * P_{\text{FS}}(t) * [\sigma_s^0 \delta(t) + I_{\text{int}}(t) + I_{\text{vol}}(t)] * P_{\text{T}}(t) \tag{3}$$

as the convolution of the sum of intensities (equation 9,12,13 in Larue et al. (2021)) with the waveform functions; the flat-surface impulse (P_{FS}), a probability density function of the surface ($pdf(t)$) and the transmitted signal power (P_{t}). For full
details of the solution method, see Larue et al. (2021).

Separation of the different backscatter components (surface, interface and volume) in equation 3 means that it is possible to
calculate their relative contributions. The backscattering coefficient of the surface and interface ($\sigma_s^0 \delta(t)$ and $\sigma_{\text{int}}^0 \delta(t)$ - equation
13 in Larue et al. (2021)) are calculated with a surface scattering model given the relevant roughness parameters (depending on
the model used). The models used in this paper are the Integral Equation Model (IEM) and Geometrical Optics (GO) model.

210 The roughness (small scale) is defined by the root-mean-square of height (s) and the correlation length (l) for IEM or in the GO case by the mean square slope ($mss = 2s^2/l^2$ assuming a Gaussian height distribution). The small-scale roughness is defined in this paper with a subscript of ice or snow (i.e s_{ice} or s_{snow}) depending on the surface they refer to. Both surface scattering models, IEM and GO, were used depending on the scale domain (for IEM: $ks < 3$ and GO: $ks \gg 1$ where k is the wavenumber). GO was also used in the Ka-band study for the surface roughness since ks was larger than 3. The three additive components:

215 ($\sigma_{\text{s}}^0\delta(t)$, I_{int}, I_{vol}) the surface, interface and volume specific intensities are calculated from components of SMRT such as permittivity models for snow and ice, microstructure representation and electromagnetic models to calculate the scattering and absorption coefficient. They are determined by the snow and ice stratigraphic and physical properties such as temperature, density, grain size (microstructure), liquid water content and salinity.

For the waveform model, spherical propagation of the wave and pulse shape is assumed based on Brown (1977) classical

220 radar theory. The power of a flat-surface impulse (P_{FS}) is defined here as equation 4 (or equation 14 in Brown (1977)):

$$P_{\text{FS}}(\tau) = \frac{G_0^2\lambda c}{4(4\pi)^2 h^3} \cdot \exp\left[-\frac{4}{\gamma}\left(\sin^2\theta + \frac{c\tau}{h\eta}\cos 2\theta\right)\right] \cdot I_0\left(\frac{4}{\gamma}\sqrt{\frac{c\tau}{h\eta}}(\sin 2\theta)\right) \tag{4}$$

with time defined as the reduced time $\tau = t - t_0$, where $t_0 = 2h/c$ is the nominal time defined as the round trip time over the distance h from the satellite to the surface. The effect of Earth's finite curvature is included by adding a factor of $\eta = (1 + h/R)$ where R is the Earth's radius and h is the satellite height (Larue et al., 2021). G_0 is = 1, λ is the satellite sensor

225 wavelength of CryoSat-2 (2.2 cm), c is the speed of light, I_0 is the modified Bessel function of the first kind at n = 0 and $\gamma = 2\sin^2(\theta_{\text{2dB}}/2)/\ln 2$, determined from the 3 dB beamwidth of the sensor. Improving to an asymmetric beamwidth in the along and across-track and a $P_{\text{T}} = \text{sinc}(\tau)$ could be consider in the future for CryoSat-2. θ is the incidence angle of the beam. In SMRT, θ is = 0 if no misalignment of the beam (off-nadir) and no local slopes are present. On sea ice, local slope is assumed to be 0. For the purposes of this paper, perfect nadir is assumed for modelling. This yields P_{FS} being equal to equation 5.

230 $$P_{\text{FS}}(\tau) = \frac{G_0^2\lambda c}{4(4\pi)^2 h^3} \cdot \exp\left[-\frac{4c\tau}{\gamma h\eta}\right] \tag{5}$$

A rough surface will affect both the amplitude and the decay of the return. The waveform will have a stronger return coming from the side lobes (off-nadir) leading to a lower amplitude and slower decay. A smooth surface will have a strong return mostly from the nadir components leading to a stronger amplitude and a faster decay. This is usually taken into account by a decrease of backscatter as a function of the incidence angle using a parametrization of small-scale roughness in $P_{\text{FS}}(\tau)$ (Brown,

235 1977; Kurtz et al., 2014; Landy et al., 2019). However, SMRT altimetry calculates the decrease of backscatter as a function of incident angle in a physical way by computing surface and interface backscatter over different off-nadir incidence angles. In a similar fashion, the small-scale roughness also controls the decay of the waveform. To allow the backscattering efficiency and computation of multiple incident angles, the theta_inc_sample parameter in SMRT was set to 8 to sample over multiple incident angles and take into account the decrease of backscatter as a function of incident angle. It can also be set to 16 or 32,

240 or any divisible number of the total gate, but increases computation time as the sampling increases.

Also, the scattering surface roughness at the footprint scale (σ_{surf}) is represented through a probability distribution function:

$$pdf(\tau) = \frac{1}{\sqrt{2\pi}(2\sigma_{\text{surf}}/c)} \exp\left(\frac{-\tau^2}{2(2\sigma_{\text{surf}}/c)^2}\right) \tag{6}$$

currently assumed to be Gaussian in SMRT. The σ_{surf} is the large-scale roughness (1 km) of the sea ice in the footprint which is different than s or l that affect surface scattering. A log-normal probability distribution (Landy et al., 2020) function may be more representative over snow-covered sea ice but has yet to be implemented in SMRT. Values of σ_{surf} are usally between 10 and 30 cm (Landy et al., 2020) and the $pdf(\tau)$ term becomes negligible under 10 cm. Future improvements of this term would add a surface backscatter response as a function of the incidence angle (Dinardo et al., 2018) and consider surface type like leads with high specular returns.

The transmitted signal power is approximated with a Gaussian function and $\sigma_p = 0.513\Delta t$:

$$P_{\text{T}}(\tau) = \frac{1}{\sqrt{2\pi}\sigma_{\text{p}}} \exp\left(\frac{-\tau^2}{2\sigma_{\text{p}}^2}\right) \tag{7}$$

where Δt is the inverse of the sensor pulse bandwidth.

2.3.2 Simulation Approach

Simulations of mean waveform for each location; Alert-17, Eureka-16/22 and CB-22 were compared with the mean of CryoSat-2 observed waveforms per location. All simulations use in-situ SMP measurements of snow properties as described in Section 2.3.3. This allowed snow variability from multiple snow surveys to be incorporated in SMRT simulations. We then found the normalisation factor for the sensor (CryoSat-2), due to the imprecise calibration of the altimeters, and optimized the small-scale roughness of sea ice (s_{ice} and l_{ice}) with the backscattering coefficient per location.

2.3.3 Simulation Parameters

Snow depth, density and SSA profiles were derived from SMP observations and used to simulate a waveform for each profile. A rolling median was applied to extract density and SSA from the SMP measurements at vertical resolutions suitable for SMRT input. For the simulations in this study, an exponential microstructure model was used. The modified Debye equation was used to calculate the microwave grain size (l_{mw}) using the Porod length l_{p} and polydispersity (K) following the approach form Picard et al. (2022):

$$l_{\text{mw}} = Kl_{\text{p}} = K\frac{4(1-\rho_{\text{s}}/\rho_{\text{i}})}{\rho_{\text{i}}SSA} \tag{8}$$

where ρ_{s} is the snow density, ρ_{i} is the density of ice. The polydispersity was set using grain type from a SMP predicted grain type classifier(rounded, faceted or depth hoar) for snow on sea ice King et al. (2020). K was assumed to be 0.7 for rounded and faceted and $K = 1.3$ for depth hoar (Picard et al., 2022). Usually, snow salinity of upper layers is minimal (< 1 PSU) and increases to 1-20 PSU for the basal layers next to sea ice (Nandan et al., 2017; Geldsetzer et al., 2009). Measured values in CB-22 were < 1 PSU for upper layers. Basal layers had an averaged of 9.3 ± 3.5 PSU for CB-22 and 10.6 ± 5.5 PSU

270   for Eureka-22. Alert-17 and Eureka-16 had lower salinity with a mean basal layer of 3 PSU for Eureka-16 and 0 PSU for Alert-17. FYI has higher salinity due to brine expulsion from the sea ice where MYI snow basal layer is much fresher since the brine expulsion is flush by melt (Nandan et al., 2017). Snow salinity increases the microwave absorption leading to stronger attenuation in saline snow than fresh snow. Snow salinity was set to the measured values and the saline snow permittivity model from Geldsetzer et al. (2009) was used.

275   Sea ice scattering in SMRT is assumed to be brine scatterers within a pure ice background for first-year ice (FYI) and air bubble scatterers within a slightly saline ice background for multiyear ice (MYI). For FYI, the density of the pure ice background is set to $917 \, \text{kg/m}^3$, for MYI the density is reduced to $880 \, \text{kg/m}^3$ by modifying the volume fraction of air/ice (Laxon et al., 2013). For both cases, scatterers within the sea ice were assumed to be spheres of radius 1 mm. Sea ice temperature of 260 K was set for the simulation. The thickness of FYI was set to 2 m and MYI was 3 m in the simulations, with a water

280   substrate underneath both. The ice salinity was set using the relation from Cox and Weeks (1974) (salinity = 7.88 - 1.59 x thickness) using the ice thickness set for both ice types (FYI: 4.7 PSU, MYI: 3.1 PSU).

    The roughness of snow and sea ice (Figure 4) is defined in the modelling of altimeter waveforms at two different scales: footprint scale (> 5 m) or radar scale (< 5 m) as defined in Landy et al. (2020). Roughness measurements in the CB-22 and Eureka-22 campaigns focused on roughness parameters at the radar scale (referred to small-scale hereafter). Two parameters (s

285   and l) define the interaction of electromagnetic waves at the radar scale where snow and ice roughness are comparable to, or less than the wavelength (2.2 cm for CryoSat-2). Previous values measured on FYI and MYI by a small-scale LIDAR experiment s_{ice} ranged from 1 to 6 mm depending on the detrending procedure (Landy et al., 2015). The large-scale (or kilometer scale) roughness is observed from 1 to 100 cm and considers melt hummocks, pressure ridges or other large-scale deformation of the ice surface. Although not evaluated for this project, some of our field measurements contained such large features that could

290   potentially overestimate the small-scale roughness. This will be discussed further as these features were found in our field experiment for rough sea ice (Figure 4). Large scale roughness σ_{surf}, represents the height standard deviation of the surface within the altimeter footprint ($\approx 1 km^2$) assuming a probability density function for the surface (Landy et al., 2020). SMRT assumes a Gaussian distribution for the surface and $\sigma_{\text{surf}} = 0.14$ m for FYI and $\sigma_{\text{surf}} = 0.22$ m for MYI from Table 2 in Landy et al. (2020) were used in simulations. These values were obtained from airborne radar surveys of the sea ice surface in Landy

295   et al. (2019) and were used for the large-scale roughness of all sites in this study.

    Measured roughness parameters shown in Table 2 present mean values for flat ice, rough ice and snow surfaces. Figure 4 shows the bivariate distribution with parameters (s, l) for the three different surfaces and shows two distinct regions for the sea ice and similar values for snow. We would suggest that the rough ice (Figure 1c) measurements with a roughness 15 times larger, contributes more to the parameters σ_{surf} at the larger scale.

300 2.3.4 Normalisation

SMRT simulations of the altimeter waveform provide the ratio between received and emitted powers, neglecting the atmospheric transmission and assuming an antenna gain $G_0 = 1$. To compare with the satellite observations that lack of precise calibration, a normalisation is necessary. A similar method of Larue et al. (2021) was applied here, which is a least squares
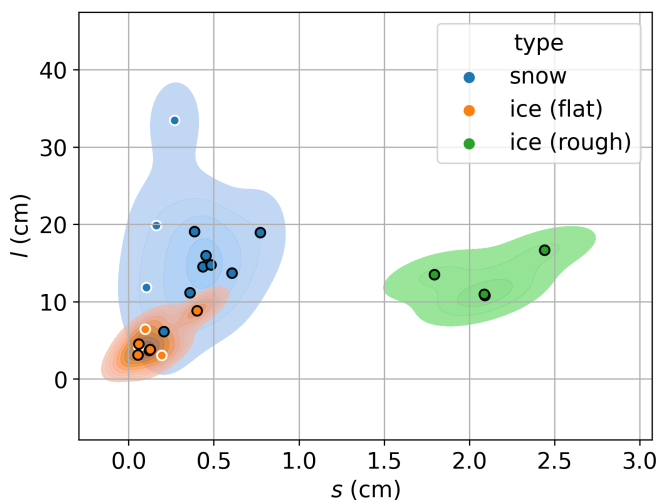
Figure 4. a) Snow surface (n = 11), b) flat sea ice (n = 9) and c) rough sea ice (n =3). d) 2D Kernel density estimate of roughness parameters measured (l, s) of the surface in a), b) and c). Black outline indicates a measurement from CB-22 and white outline for Eureka-22.

surface	s (mm)	l (cm)	n	n_{sub} (n x 20)
snow	3.9 ± 1	16.3 ± 3.4	11	160
flat sea ice	1.4 ± 0.6	4.7 ± 0.1	9	100
rough sea ice	21.0 ± 1.3	13.0 ± 1.4	3	60

Table 2. Overview of the measured roughness parameters. Rough sea ice had a mean small scale rms (s) of 21.0 mm, snow had 3.9 mm and flat sea ice had 1.4 mm

regression fit to the observations. The Normalisation factor in watts (Λ) calculated across all sites assuming the satellite cali-
305 bration is constant between the acquisition. The Λ in Watts is multiplied to the simulation (unitless) to match the observation
in Watts (power received by the sensor).

In their study over Antarctica, Larue et al. (2021) were able to use data over several months (at least 50 observations at
each of seven sites) due to slowly changing snow microstructure. Data were also filtered for $\pm$ 1 gate tolerance. Here, data
are much more limited and only obvious outliers were excluded. For the final calculation of the normalisation factor, all
310 observed waveforms per site were aligned to the same nominal gate as the simulation, then averaged together to yield one

mean waveform. This allowed a proper calculation of the normalisation factor between the simulated and observed. The Λ is part of the optimization of the small-scale roughness.

2.4 Roughness Optimisation

The small scale-roughness of snow and ice impacts the total power measured by the altimeter (equation 3). The reflection at

315   each rough interface is represented by IEM or GO surface models and the roughness values are key in modelling the backscatter. The small scale-roughness was measured only for CB-22 and Eureka-22 and yielded distinct values for flat and rough ice. It is unclear whether the values measured spatially represent the true roughness. For this reason, the s and l of both the sea ice and snow (will be optimized per campaign (Eureka-16, Alert-17, Eureka-22 and CB-22) using a least-square fit of the residual between the observed and simulated waveforms and then compared with measured values from this study and Landy et al.

320   (2015a). To simplify the optimization, the roughness of the sea ice and snow are equal ($s_{snow} = s_{ice} = s$ and $l_{snow} = l_{ice} = l$). Also, we focused on optimizing the small-scale roughness since it affects the simulated waveform the most.

Since the Λ influences the amplitude of the simulated power, normalisation was estimated in the optimization along the roughness parameters. The optimized range for s was 1 to 10 mm and 1 to 40 cm for l based on Landy et al. (2019) and our measured values. The optimization was done in two steps: 1) the Λ and roughness parameters for all sites were found, 2) Λ

325   is fixed and the roughness for each site were optimized with initial roughness from 1). The optimization of the waveform was based on the least square residuals of the log transform simulation and observed data. To evaluate our fit, the norm squared of the residuals (n_{res}) was used as a metric. Fons and Kurtz (2019) defined a good waveform fit when (n_{res}) < 0.3. The gates 0 to 160 before the nominal return at gate 164 were removed from the fit to reduce the influence of noise. The nominal gate is the gate at which SMRT will simulate the surface.

3 Results

330

3.1 SMRT Evaluation

In this section, the waveforms modeled by SMRT using the measured snow parameters driven from SMP measurements were evaluated at all sites. The observed waveforms from CryoSat-2 at Eureka-16/22, Alert-17 and CB-22 are shown with dashed lines in Figure 5. The amplitude of Alert-17 (MYI) was lower than the amplitude of CB-22 and Eureka-22 (FYI). Eureka-16

335   composed of a mixture of FYI and MYI has a higher amplitude than Alert-17 but lower than CB-22 and Eureka-22. The amplitude decay or the slope of the trailing edge (TES, Table 3) on the log scale showed a different decay between CB-22/Eureka-22 and Alert-17/Eureka-16.

SMRT simulations of CryoSat-2 waveforms are also shown in Figure 5 for each site with the normalisation factor of Λ = 5.9×10^8 W (Table 3). Poor fit using a constant roughness for all sites was obtained (not shown here). Simulations with

340   optimized roughness are shown in Figure 5 with optimized roughness parameters shown in Table 3.
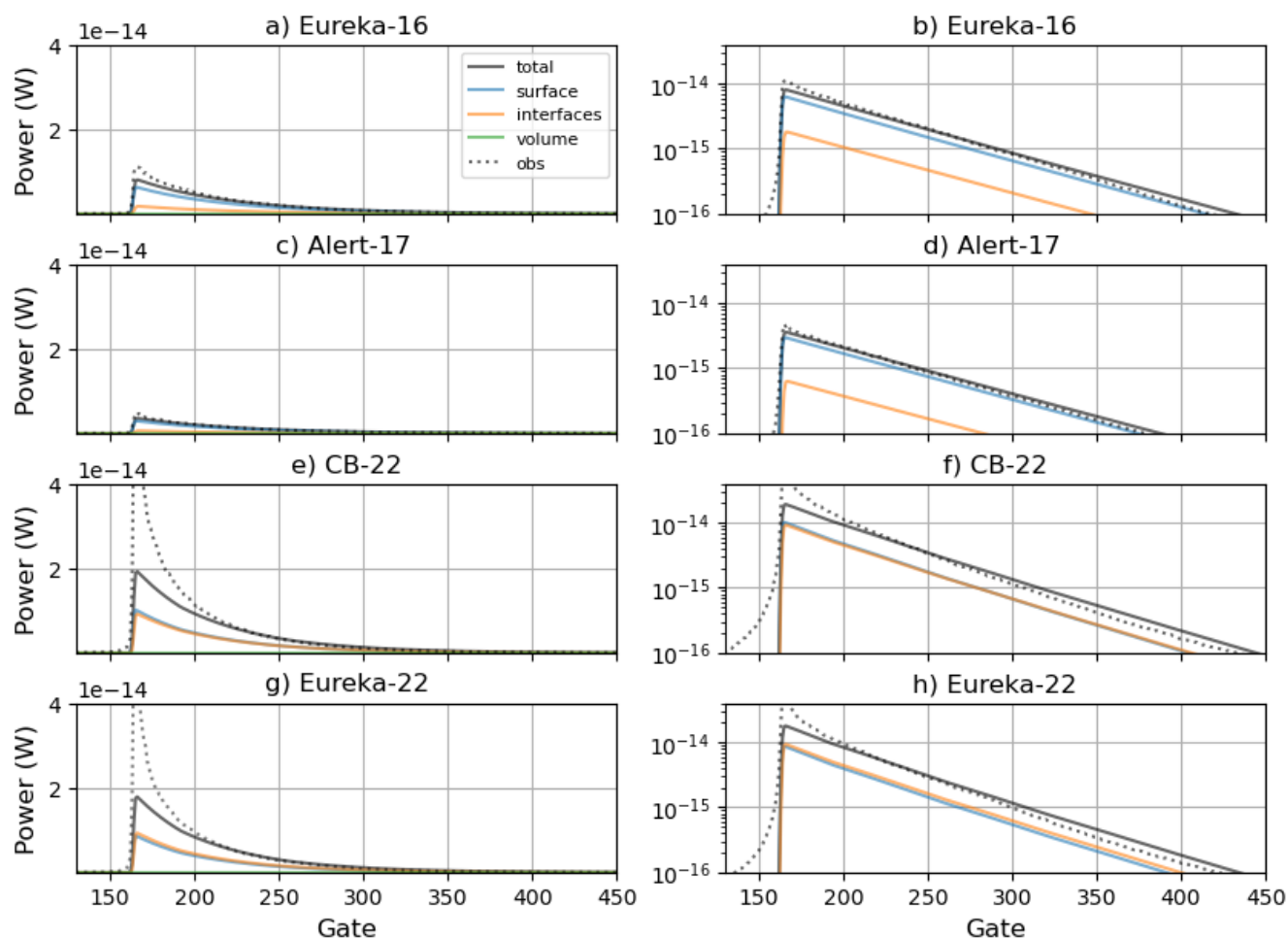
Figure 5. Comparison between simulated and observed CryoSat-2 waveforms for Alert-17, Eureka-16/22 and Cambridge Bay with a normal-isation factor, 5.9×10^8 W. Simulated waveforms are shown by a black solid line and observation by dotted lines. The different contributions of the received power are also shown by colored solid lines. The right-hand side column is a linear scale and the left-hand side is a logarithmic scale of the power.

The optimized roughness per site (Table 3) yielded lower s values for CB-22 = 2.1 mm and Eureka-22 = 1.6 mm and rougher sea ice for Eureka-16 = 4.9 mm and Alert-17 = 5.6 mm. The optimized value for FYI in CB-22 and Eureka-22 (2.1 mm and 1.6 mm) was similar to the measured value (1.4 mm, Table 2). The l yielded the maximum value of the optimized range for all sites. A rougher ice surface was needed for Alert-17 and Eureka-16, which is consistent with the MYI characteristics for Alert-17 and mixed MYI/FYI characteristics for Eureka-16 (Figure 1). Overall, the n_{res} showed a good fit was obtained when the roughness was optimized but the peakiness was underestimated and was particularly prominent in the absolute backscatter for pure FYI sites.

Site	s (mm)	l (cm)	n_{res}	TES
CB-22	2.1	40	0.33	-0.021
Eureka-22	1.6	40	0.27	-0.021
Eureka-16	4.9	40	0.02	-0.018
Alert-17	5.6	40	0.04	-0.017
Normalisation factor: $\Lambda = 5.9 \times 10^8$ W				

Table 3. Overview of the optimized roughness parameters, waveforms fit parameters and the normalisation factor.

The contribution of the backscatter sources i.e. snow surface, internal interfaces (including snow-ice interface), and snow volume ($\sigma_s^0 \delta(t)$, $I_{\text{int}}(t)$ and $I_{\text{vol}}(t)$ in equation 3) to the total backscatter were also shown. A mixture of equal returns from 350 the surface and the interface was obtained for CB-22 and Eureka-22 (FYI) and returns dominated by the surface for Alert-17 and Eureka-16. The contribution from the surface reflection affected all sites. This means that for Ku-band, backscatter was dominated by changes in the permittivity of snow and ice layers, which increased reflectivity between layers, and the roughness of the surface/interface. Volume scattering is minimal at Ku-Band.

3.2 Sensitivity analysis

355 After optimization and evaluation of the SMRT simulated waveforms, we investigated the effect of simulation parameters on 1) the total simulated power and 2) the power contribution simulated by SMRT. First, a sensitivity analysis was carried out on the total power to identify parameter accuracy constraints. These results were shown in Figure 6 for Ku-band and Figure 7 for Ka-band, based on measured values from SMP profiles. We selected CB-22 and Alert-17 as they both were representative of FYI and MYI respectively. The mean simulations using in-situ parameters (same as Figure 5) were shown as the solid line for 360 CB-22 and Alert-17 profiles. Modification of parameters was shown by dotted and dashed lines (reduction or increase from the measured parameters).

In Figure 6, the parameters that were used in the calculation of both snow and sea ice permittivities (snow density, snow temperature, snow salinity, sea ice salinity and sea ice temperature) all had an effect on the amplitude. This can be noted from Figure 6 c), d) and e) because the temperature, density and salinity affect the permittivity of snow in SMRT. Snow salinity 365 only affected CB-22 since saline snow is not present on MYI (Alert-17). In h), volume fractions (driven by brine concentration / salinity for FYI and ice density for MYI) and temperatures of sea ice had a smaller but notable impact on the amplitude. The snow parameters affecting the most the amplitude was the density and the salinity. Snow depth also affects the amplitude as it impacts the number of snow layers (Figure 6 a). Snow thickness only impacted CB-22 since most of Alert-17 reflected power comes from the surface. For the roughness, it can be seen from Figure 6 f) and g) that the roughness greatly affects the 370 amplitude. The roughness also affects the decay of the waveform. Variation in snow SSA did not effect the total amplitude. Averaging to a 1-layer model also affected the amplitude.
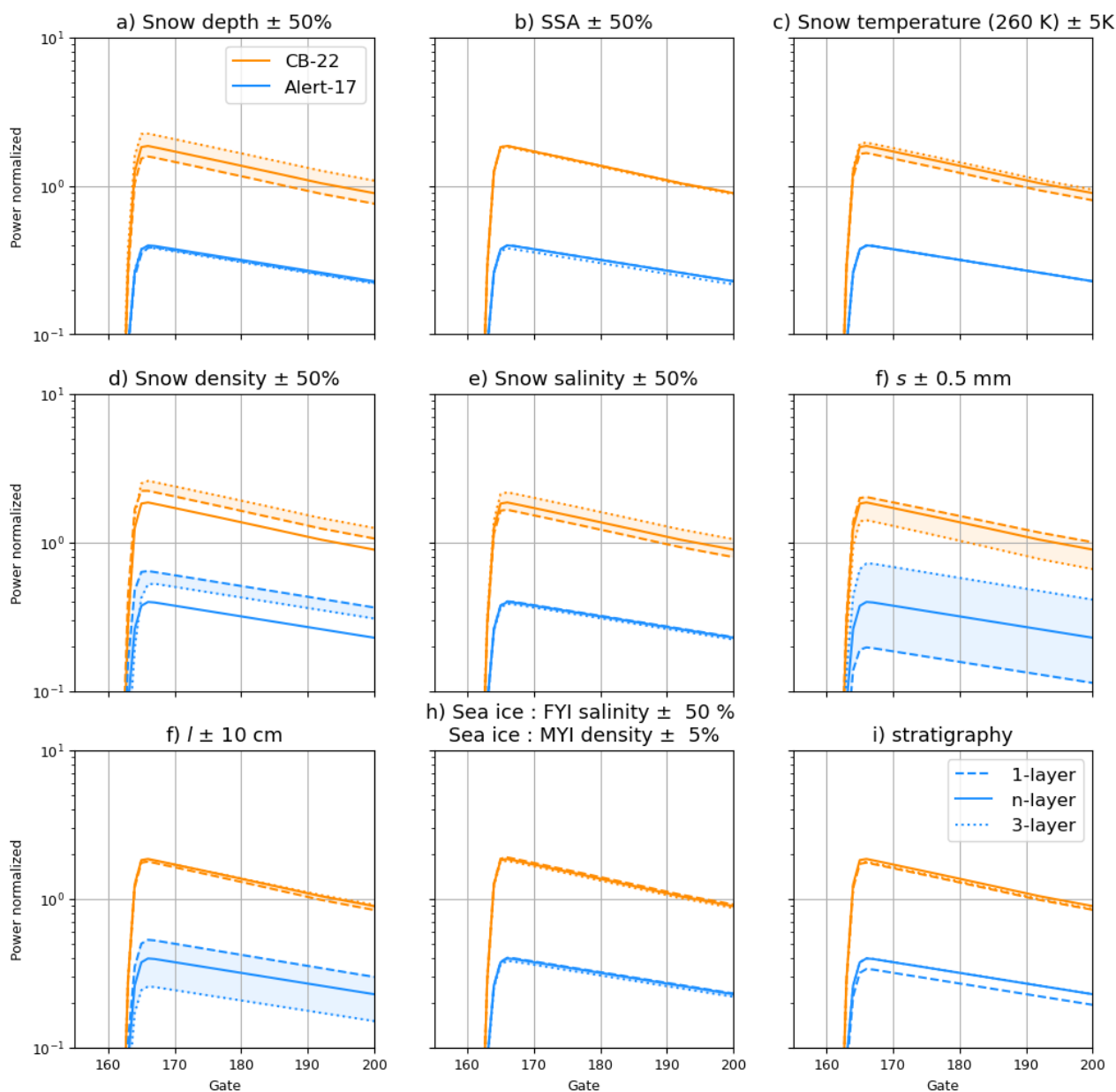
Figure 6. Ku-band sensitivity analysis around the mean measured parameters used to drive SMRT simulations for CB-22 and Alert-17. The solid line is the mean simulation, the dotted line is the negative change and the dashed is the positive change.

For Ka-band (Figure 7), a similar sensitivity to snow parameters was found. Snow depth did effect the amplitude of both sites. Again, a strong sensitivity to snow density for both CB-22 and Alert-17 was observed. For Alert-17, sensitivity to SSA can be observed even if no volume scattering contribution was simulated. This is due to the basal layer of depth hoar in Alert-17
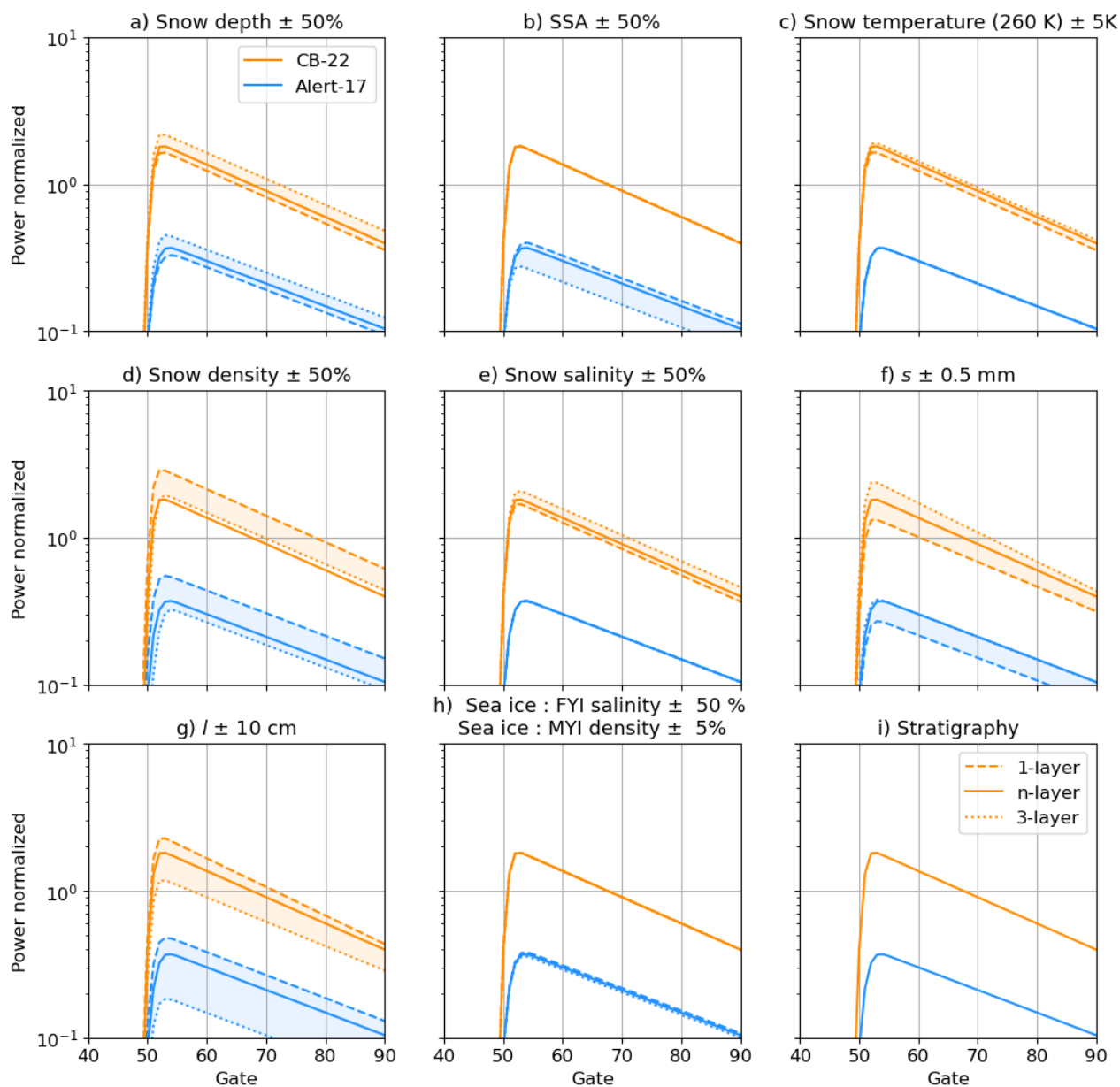
Figure 7. Ka-band sensitivity analysis around the mean measured parameters used to drive SMRT simulations for CB-22 and Alert-17. The solid line is the mean simulation, the dotted line is the negative change and the dashed is the positive change.

375   scattering the reflection from the interface which is likely to reduce the total backscatter. This effect was not present at Ku-band due to larger wavelength where the interaction with the snow grain is lesser.

In Figure 8, the effect of roughness parameters on the backscatter contribution was investigated. It showed that the influence of both surfaces (snow and ice) on the total power depends on the small-scale roughness. For Ku-band, interface and surface reflection were similar for low roughness ($s < 2$ mm) but surface reflection dominated as s increased. For Ka-band using GO,
380 the surface is dominating but the interface still was $\geq= 20$ % for both sites.
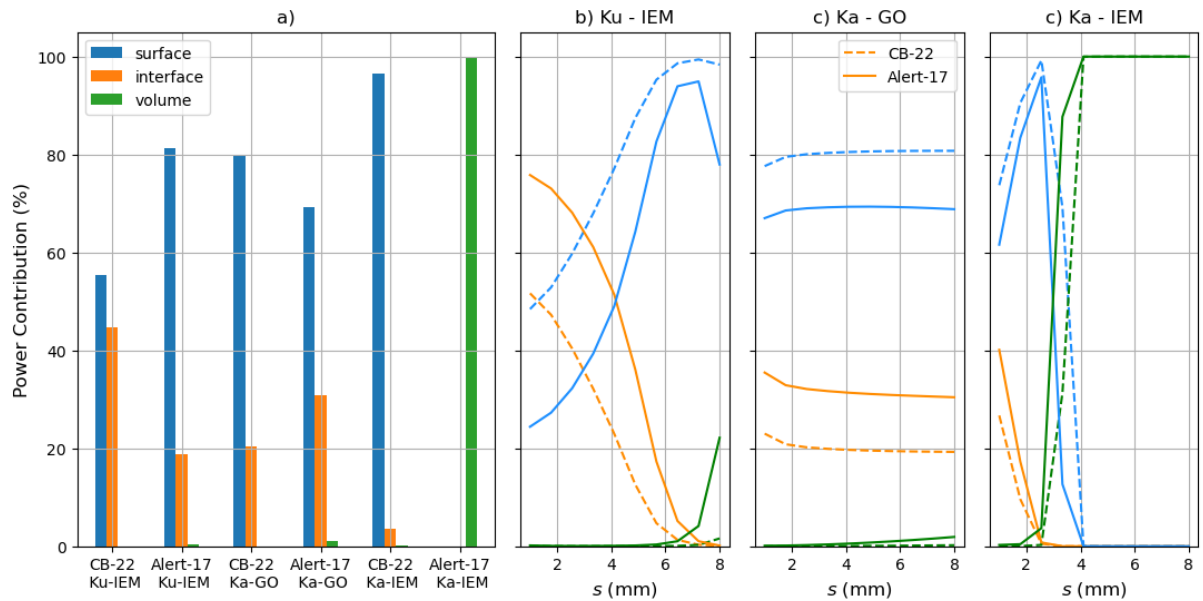
Figure 8. a) Contribution of total power from reflection of the surface, ice interface and volume scattering for CB-22 and Alert-17 for Ku and Ka-band. The contribution as a function of the s is shown in b) for Ku with IEM, c) for Ka with GO and d) for Ka with IEM.

At Ka-band, it is important to mention that $ks > 3$ if $s > 4$ mm and the surface model used was GO compared to IEM for Ku since $s = 5.6$ mm for Alert-17. Technically, this is at the limit of the IEM regime. However, the roughness was optimized for Ku-band waveform so it is risky to apply the same roughness for both bands. Figure 8 d) also showed if IEM was used instead, the contribution for Alert-17 at Ka-band becomes 100 % volume scattering. This result is relevant for the CRISTAL mission
385 and highlights the importance of knowing the roughness to derive snow thickness, and of roughness parameterization in SMRT for altimeter applications.

Finally, in Figure 9, the effect of the microstructure and salinity was investigated on the contribution. Here, GO was used for Ka-band. The SSA was varied by $\pm$ 50 % from the measured values. The backscatter contribution varied by 40 % for Ka-band at Alert-17. Again, this is because lowering the SSA of the depth hoar layer increased the divergence of the radar wave reaching
390 the base of the snowpack which ultimately reduced the contribution of the ice interface. A similar effect is seen for salinity at CB-22. The brine in the snow absorbs the radar wave reaching the base of the snowpack which also reduces the contribution of the ice interface as salinity increases.
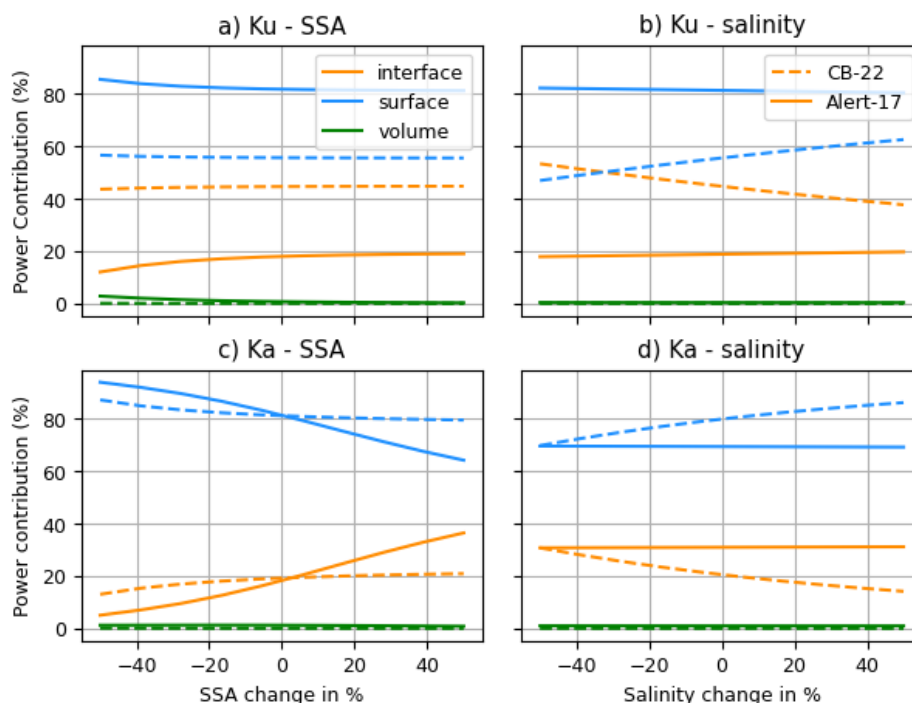
Figure 9. Sensitivity of the SSA and salinity of snow on the power contribution (%) from the surface, ice interface and volume scattering.

3.3 Micro-CT

Finally, we investigated how the high resolution micro-CT measurements of snow used as inputs into SMRT affected the
simulations across the 4 sites in CB-22 (AK1-AK4). Figure 3 a) shows the difference in measurement between the traditional
pit, SMP at two different resolutions and micro-CT measurements. In terms of simulation, the amplitude was underestimated by
the pit and SMP low resolution (5 cm) measurements compared with the micro-CT and SMP high resolution (1 cm). In Figure
10 b), all pit (AK1-AK4) amplitudes were smaller than micro-CT amplitudes. The SMRT simulations using different sources
of snow measurement inputs, but of the same resolution (1 and 5 cm), produced similar simulation results. The difference
between simulations was driven by the snow density since the snow depth was similar and temperature and salinity were the
same for pits, SMP and micro-CT simulations. Also, it was shown earlier that SSA or microstructure may not contribute to the
amplitude of the waveform at Ku-band (Figure 6).

4 Discussion

SMRT can successfully simulate waveforms of altimeters on sea ice with the appropriate small-scale roughness parameters,
and a normalisation factor to account for the calibration of the sensor ($\Lambda = 5.9 \times 10^9$ W). It is clear from Figure 5 that
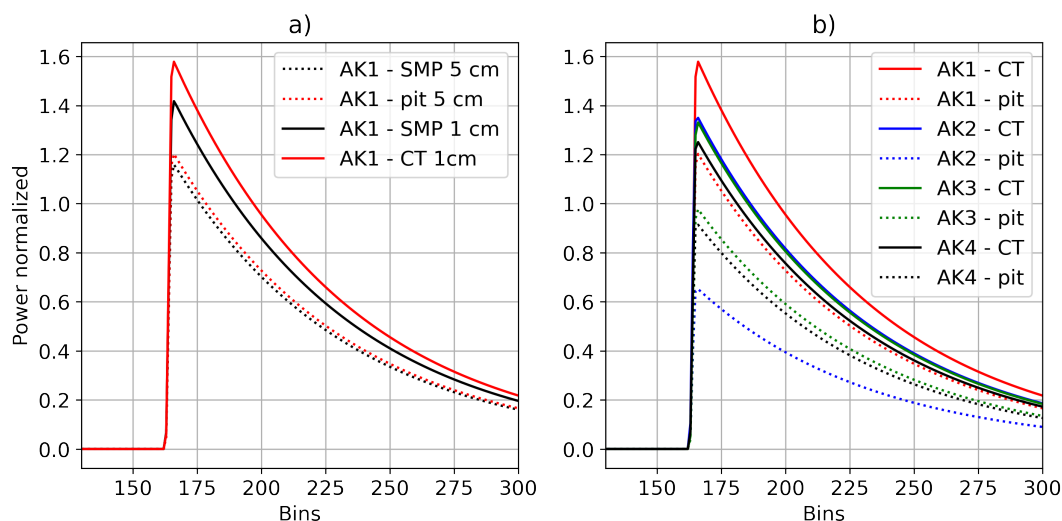
Figure 10. Comparison of SMRT simulation between instruments and processed data resolutions, a) simulations between SMP (1 cm), micro-CT (1 cm), pit (5 cm) and SMP (5 m). b) differences in simulations between pit and micro-CT at four sites in CB-22.

simulations driven only by snow-measured parameters with constant roughness parameters were insufficient to correctly model Ku-band altimeter waveforms at different sites. The site specific, optimized roughness is critical to model the amplitude and the waveform decay of the signal for different sea ice types (FYI and MYI). The roughness was the only parameter affecting the waveform decay under the assumption of no mispointing which would affect both the peak power and decay. This allows to estimate the roughness (s and l) from the observed waveform decay which is critical for sea ice thickness retrieval (Landy et al., 2020).

Knowledge of sea ice roughness is critical to ascertain whether the radar signal is predominantly from the snow surface, ice interface, or volume scattering in the snow. When roughness was optimized (Table 3), the Ku-band signal came mostly from the snow surface and sea ice interface. For Ka-band, the signal was sensitive to the snow surface, interface and volume scattering depending on the surface model used. This highlights the importance of the roughness parameters in SMRT for altimeters.

Using the IEM surface scattering domain, optimized roughness values (Table 3) were found to be similar to previously reported measured values in the literature (Landy et al., 2015b). The measured roughness for flat ice in CB-22 and Eureka-22 (Table 2, $s = 1.4$ mm) matched closely the optimized values in CB-22 ($s = 2.1$ mm) and Eureka-22 ($s_{ice} = 1.6$ mm). Values optimized for Alert-17 ($s = 5.6$ mm) and Eureka-16 ($s = 4.9$ mm) matched values measured on FYI ($s = 3.1$ mm) and MYI ($s = 4.3$ mm) from Table 2 in Landy et al. (2015a). For Alert-17 and Eureka-16, a rougher sea ice was optimized as MYI is rougher than FYI (King et al., 2020; Fredensborg Hansen et al., 2021). For l, the optimized values for all sites ($l = 40$ cm) were much higher than the measured values ($l_{ice} = 5.2$ cm) and reached the maximum of the optimized range. Those higher values were needed to correctly simulate the faster decay. A larger correlation length should represent a smoother surface, but our measured values for flat ice were smaller than rough sea ice and snow which might indicate a potential problem in

the roughness measurement method for l. The areas investigated were potentially not large enough (horizontally) to estimate the correct length. Estimated values (s and l) are dependent on the detrending method, and a community consensus on which method to estimate roughness relevant to microwave radiative transfer is still lacking. Overall, the roughness parametrization gave an appropriate fit with the Ku-band waveform, but it is still unclear if the roughness values are realistic. The optimization and measurements of roughness are not trivial and remain the most challenging parameter to quantify in models of sea ice altimetry.

SMRT simulations showed that the radar echoes at Ku-band came from the reflection at the snow and sea ice interface and the change. Waveform amplitudes were also sensitive to snow parameters (density, temperature and salinity) that changed the effective permittivity of snow layers. This increased reflection and therefore increased the amplitude of the waveform. Sea ice parameters were also found to influence the reflection to a lesser extent as they modify the permittivity of the last interface. It can be concluded that the altimeter signal at Ku-band is sensitive to changes in the effective permittivity of the snowpack and the ice. Note that snow density also affects the speed of the wave and in turn the estimated surface elevation, which has not been investigated here. The low sensitivity to snow microstructure is likely due to the strict nadir angle used in the simulations. This behavior is different for SAR imagery with a higher incidence angle, which leads to a stronger component of volume scattering at Ku-band (King et al., 2018). This suggests that a model similar to Landy et al. (2019) that simplifies volume scattering from microstructure, but incorporates complex roughness interactions (at two scales) could be sufficient to model Ku-band altimeter.

SMRT simulations of the radar echoes from the snow surface and volume scattering at Ka-band were more prevalent than for Ku-band. The altimeter signal at Ka-band is affected by the snow density like Ku-band, but was also sensitive to the microstructure of snow which has implications for the CRISTAL mission. The signal was mostly sensitive to the snow surface but Figure 7 b) and 9 c) showed that this contribution is highly sensitive to SSA. The microstructure of snow will have to be known, approximated, or its effects minimized by retrieval algorithms since it affects the total power. Also, volume scattering by SMRT altimeter underestimated scattering at higher frequency (Ka-band) since it is a first order scattering model. Implementing higher order for multiple scattering within the snowpack and the advanced IEM (AIEM) to account for multiple scattering of the interface should be considered going forward (Larue et al., 2021).

Questions still arise on which model (IEM or GO) should be used at Ka (Figure 8 but volume scattering could potentially contribute to 100% of the total power received. The roughness set for Ka-band resulted from an optimization at Ku-band and is also on the limit of the IEM model ($ks < 3$). Further investigations are needed to understand if the return at Ka-band comes mostly from the snow surface or volume scattering (Figure 8), and in which conditions. This is crucial if we want to retrieve snow depth with CRISTAL from the difference between tracking points of Ka and Ku-band (Lawrence et al., 2018). Ground-based Frequency Modulated Continuous Wave (FMCW) radar at Ka-band could help measure the backscatter per layer leveraging a large bandwidth.

The domination of the surface signal contribution for both Ku and Ka-band is consistent with the finding from (Willatt et al., 2023) which found that the highest amplitude peak of a ground-based Radar at the Ku and Ka-band was closer to the surface than the ice.

Snow properties have an impact on the tracking point by modifying the amplitude of the radar echoes for both frequencies
460   as was shown in Figure 6 and 7. An appropriate radiative transfer model of snow will be needed to correctly infer snow depth
from tracking point differences at Ku- and Ka-band since this study showed how sensitive both frequencies were to snow
parameters. Of all snow parameters, Snow density showed the strongest influence on the amplitude of Ku- and Ka-band. This
sensitivity also opens the opportunity to improve retrieval of snow depth like Fons et al. (2023), or estimate snow density from
the waveform. This has implications for sea ice thickness retrieval because uncertainty in snow density estimates can lead to
465   bias up to 30 cm in ice thickness estimation (Kern et al., 2015).

Finally, the high resolution micro-CT snow measurements were evaluated in SMRT simulations and produced consistently
higher amplitudes for all CB-22 sites compared to low resolution pit and SMP. This is likely due to the enhanced vertical infor-
mation in snow density (Figure 3) provided by the micro-CT measurement and SMP at high resolution. Figure 3 showed large
changes in volume fraction from the CT compared to a steady decrease in density from the pit and SMP low resolution. These
470   substantial changes in density increased reflection. Nonetheless, using a 1-layer model with bulk density might underestimate
the reflection of the altimeter signal, and the non-uniform structure of the snowpack should be included in a full error budget
analysis for future radar altimeter retrieval algorithms.

Future developments of SMRT for sea ice altimetry could help mitigate issues and improve the simulations, especially
solutions to overcome the need for normalization would help better constrain the roughness and determine the respective
475   contributions of the interfaces and surface (Larue et al., 2021). Some developments include a waveform model for SAR mode,
3-phase medium (ice, air and brine) and adding multiple order scattering for Ka-band and big grains.

5   Conclusion

In this paper, we showed the capabilities of SMRT to simulate altimetric waveforms over sea ice for three different regions with
distinct ice types and snow cover over multiple seasons. SMRT showed that snow and sea ice properties had a notable impact on
480   the reflected signal (amplitude). The most critical parameter in SMRT simulation is the roughness of the sea ice since it dictates
how much power is reflected at the ice interface and the waveform decay, which could be challenging for physical retrackers.
SMRT can inform the backscatter contribution coming from either the surface, interface or volume scattering and showed for
Ka-band (Figure 8), that the signal comes mostly (> 70 %) from the snow surface if the ice roughness is large enough (s_ice
> 2.0 mm), which is encouraging for snow depth retrieval and the CRISTAL mission. However, considering snow properties
485   with a physical retracker will be necessary since snow properties shift the tracking point for both frequencies (Figure 6 and 7).
SMRT could improve retrieval of snow depth, snow density and ice thickness using the model as a base for a physical retracker
for the CRISTAL mission. This study improved our understanding of the interaction between the radar altimeter signal with
sea ice by using a radiative transfer approach based on state-of-the-art in-situ snow measurements.

Code and data availability. Code for this paper are available at https://github.com/JulienMeloche/AKROSS_paper.

490 SMRT commit version = 1.3.

Data from CB-22 (AKROSS) is available at DOI: 10.5281/zenodo.11205157.

Data from Eureka-22 is available at (to be added).

Data from Alert-17 and Eureka-16 is available at DOI: 10.5281/zenodo.4068349 and DOI: 10.5281/zenodo.11210316.

Appendix A: List of Symbols

L	mean distance between structural elements in 3D
$\tilde{F}$	median of the penetration resistance force
d_i	SMP specific surface area coefficients
Δt	time
$P_r(t)$	Returned power at the Radar
$P_t(t)$	Transmitted power of the Radar
$pdf(t)$	probability density function of the surface
$P_{FS}(t)$	Flat surface impulse
σ_s^0	backscattering coefficient of the surface
$\delta(t)$	dirac delta function
I_{int}	specific intensities from interface reflection
I_{vol}	specific intensities from volume scattering
mss	mean square slope
s	small scale rms height of the ice or snow surface (s_{ice} or s_{snow})
l	small scale correlation length of the ice or snow surface (l_{ice} or l_{snow})
σ_{surf}	large scale rms height of the surface
G_0	peak antenna gain at boresight
h	height of satellite
λ	wavelength of the sensor
θ	incident angle
c	speed of light
R	radius of the Earth
I_0	first component of the Bessel function
l_{mw}	microwave microstructural lenght
l_p	porod length
ρ_s	density of snow
ρ_i	density of ice
κ	polydispersity of snow
Λ	normalisation factor
A_i	Amplitude of the waveform i

495

Author contributions. JM wrote the manuscript with contributions from all co-authors. MS, HL and NR designed the experiment. JM, MS, HL and GP performed the analysis. JM, MS, HL, NR, RE, RS, PT, JK and AL collected the field measurements. MJ and HL analysed and developped the Micro-CT data and protocol. GP wrote the code of the model used. JB, AB and MS provided provided guidance with the CryoSat-2 data. All co-authors reviewed the manuscript and provided analysis guidance.

Competing interests. Some authors are members of the editorial board of The Cryosphere.

Acknowledgements. This work was funded under the ESA AKROSS project, ESA CONTRACT NO. 4000130073/20/I-DT and was only possible thanks to extensive logistical the Canadian High Arctic Research Station (particularly Martin Leger) and Polar Knowledge Canada. The authors would also like to thank Adrià Blanco (University of Victoria), John Yackel, Hoi Ming Lam and Monojit Saha (University of Calgary), and the whole GRIMP team from Sherbrooke in particular Charlotte Crevier and Caroline Dolant for the shipping of dangerous goods and Juliette Ortet for her tea etiquette.

References

Allard, R. A., Farrell, S. L., Hebert, D. A., Johnston, W. F., Li, L., Kurtz, N. T., Phelps, M. W., Posey, P. G., Tilling, R., Ridout, A., and Wallcraft, A. J.: Utilizing CryoSat-2 Sea Ice Thickness to Initialize a Coupled Ice-Ocean Modeling System, Advances in Space Research, 62, 1265–1280, https://doi.org/10.1016/j.asr.2017.12.030, 2018.

Blockley, E. W. and Peterson, K. A.: Improving Met Office Seasonal Predictions of Arctic Sea Ice Using Assimilation of CryoSat-2 Thickness, The Cryosphere, 12, 3419–3438, https://doi.org/10.5194/tc-12-3419-2018, 2018.

Brown, G.: The Average Impulse Response of a Rough Surface and Its Applications, IEEE Transactions on Antennas and Propagation, 25, 67–74, https://doi.org/10.1109/TAP.1977.1141536, 1977.

Cox, G. F. N. and Weeks, W. F.: Salinity Variations in Sea Ice, Journal of Glaciology, 13, 109–120, https://doi.org/10.1017/S0022143000023418, 1974.

Derksen, C., Burgess, D., Duguay, C., Howell, S., Mudryk, L., Smith, S., Thackeray, C., and Kirchmeier-Young, M.: Changes in Snow, Ice, and Permafrost across Canada; Chapter 5 in Canada's Changing Climate Report, Tech. rep., https://doi.org/10.4095/314614, 2019.

Dinardo, S., Fenoglio-Marc, L., Buchhaupt, C., Becker, M., Scharroo, R., Joana Fernandes, M., and Benveniste, J.: Coastal SAR and PLRM Altimetry in German Bight and West Baltic Sea, Advances in Space Research, 62, 1371–1404, https://doi.org/10.1016/j.asr.2017.12.018, 2018.

Fan, Y., Li, L., Chen, H., and Guan, L.: Evaluation and Application of SMRT Model for L-Band Brightness Temperature Simulation in Arctic Sea Ice, Remote Sensing, 15, 3889, https://doi.org/10.3390/rs15153889, 2023.

Ferraro, E. J. and Swift, C. T.: Measuring Geophysical Parameters of the Greenland Ice Sheet Using Airborne Radar Altimetry, Journal of Glaciology, 41, 607–618, https://doi.org/10.3189/S0022143000034924, 1995.

Fons, S., Kurtz, N., and Bagnardi, M.: A Decade-plus of Antarctic Sea Ice Thickness and Volume Estimates from CryoSat-2 Using a Physical Model and Waveform Fitting, The Cryosphere, 17, 2487–2508, https://doi.org/10.5194/tc-17-2487-2023, 2023.

Fons, S. W. and Kurtz, N. T.: Retrieval of Snow Freeboard of Antarctic Sea Ice Using Waveform Fitting of CryoSat-2 Returns, The Cryosphere, 13, 861–878, https://doi.org/10.5194/tc-13-861-2019, 2019.

Fredensborg Hansen, R. M., Rinne, E., and Skourup, H.: Classification of Sea Ice Types in the Arctic by Radar Echoes from SARAL/AltiKa, Remote Sensing, 13, 3183, https://doi.org/10.3390/rs13163183, 2021.

Geldsetzer, T., Langlois, A., and Yackel, J.: Dielectric Properties of Brine-Wetted Snow on First-Year Sea Ice, Cold Regions Science and Technology, 58, 47–56, https://doi.org/10.1016/j.coldregions.2009.03.009, 2009.

Goosse, H., Kay, J. E., Armour, K. C., Bodas-Salcedo, A., Chepfer, H., Docquier, D., Jonko, A., Kushner, P. J., Lecomte, O., Massonnet, F., Park, H.-S., Pithan, F., Svensson, G., and Vancoppenolle, M.: Quantifying Climate Feedbacks in Polar Regions, Nature Communications, 9, 1919, https://doi.org/10.1038/s41467-018-04173-0, 2018.

Guerreiro, K., Fleury, S., Zakharova, E., Rémy, F., and Kouraev, A.: Potential for Estimation of Snow Depth on Arctic Sea Ice from CryoSat-2 and SARAL/AltiKa Missions, Remote Sensing of Environment, 186, 339–349, https://doi.org/10.1016/j.rse.2016.07.013, 2016.

Haas, C., Beckers, J., King, J., Silis, A., Stroeve, J., Wilkinson, J., Notenboom, B., Schweiger, A., and Hendricks, S.: Ice and Snow Thickness Variability and Change in the High Arctic Ocean Observed by In Situ Measurements: Arctic Sea Ice and Snow Thickness, Geophysical Research Letters, 44, 10,462–10,469, https://doi.org/10.1002/2017GL075434, 2017.

Hayne, G.: Radar Altimeter Mean Return Waveforms from Near-Normal-Incidence Ocean Surface Scattering, IEEE Transactions on Antennas and Propagation, 28, 687–692, https://doi.org/10.1109/TAP.1980.1142398, 1980.

Kern, M., Cullen, R., Berruti, B., Bouffard, J., Casal, T., Drinkwater, M. R., Gabriele, A., Lecuyot, A., Ludwig, M., Midthassel, R.,
545   Navas Traver, I., Parrinello, T., Ressler, G., Andersson, E., Martin-Puig, C., Andersen, O., Bartsch, A., Farrell, S., Fleury, S., Gascoin, S.,
       Guillot, A., Humbert, A., Rinne, E., Shepherd, A., Van Den Broeke, M. R., and Yackel, J.: The Copernicus Polar Ice and Snow Topography
       Altimeter (CRISTAL) High-Priority Candidate Mission, The Cryosphere, 14, 2235–2251, https://doi.org/10.5194/tc-14-2235-2020, 2020.

Kern, S., Khvorostovsky, K., Skourup, H., Rinne, E., Parsakhoo, Z. S., Djepa, V., Wadhams, P., and Sandven, S.: The Impact of Snow Depth,
       Snow Density and Ice Density on Sea Ice Thickness Retrieval from Satellite Radar Altimetry: Results from the ESA-CCI Sea Ice ECV
550   Project Round Robin Exercise, The Cryosphere, 9, 37–52, https://doi.org/10.5194/tc-9-37-2015, 2015.

King, J., Derksen, C., Toose, P., Langlois, A., Larsen, C., Lemmetyinen, J., Marsh, P., Montpetit, B., Roy, A., Rutter, N., and Sturm, M.: The
       Influence of Snow Microstructure on Dual-Frequency Radar Measurements in a Tundra Environment, Remote Sensing of Environment,
       215, 242–254, https://doi.org/10.1016/j.rse.2018.05.028, 2018.

King, J., Howell, S., Brady, M., Toose, P., Derksen, C., Haas, C., and Beckers, J.: Local-Scale Variability of Snow Density on Arctic Sea Ice,
555   The Cryosphere, 14, 4323–4339, https://doi.org/10.5194/tc-14-4323-2020, 2020.

Kurtz, N. T., Galin, N., and Studinger, M.: An Improved CryoSat-2 Sea Ice Freeboard Retrieval Algorithm through the Use of Waveform
       Fitting, The Cryosphere, 8, 1217–1237, https://doi.org/10.5194/tc-8-1217-2014, 2014.

Kwok, R.: Simulated Effects of a Snow Layer on Retrieval of CryoSat-2 Sea Ice Freeboard, Geophysical Research Letters, 41, 5014–5020,
       https://doi.org/10.1002/2014GL060993, 2014.

560   Landy, J. C., Isleifson, D., Komarov, A. S., and Barber, D. G.: Parameterization of Centimeter-Scale Sea Ice Surface Roughness Using
       Terrestrial LiDAR, IEEE Transactions on Geoscience and Remote Sensing, 53, 1271–1286, https://doi.org/10.1109/TGRS.2014.2336833,
       2015a.

Landy, J. C., Komarov, A. S., and Barber, D. G.: Numerical and Experimental Evaluation of Terrestrial LiDAR for Parame-
       terizing Centimeter-Scale Sea Ice Surface Roughness, IEEE Transactions on Geoscience and Remote Sensing, 53, 4887–4898,
565   https://doi.org/10.1109/TGRS.2015.2412034, 2015b.

Landy, J. C., Tsamados, M., and Scharien, R. K.: A Facet-Based Numerical Model for Simulating SAR Altimeter
       Echoes From Heterogeneous Sea Ice Surfaces, IEEE Transactions on Geoscience and Remote Sensing, 57, 4164–4180,
       https://doi.org/10.1109/TGRS.2018.2889763, 2019.

Landy, J. C., Petty, A. A., Tsamados, M., and Stroeve, J. C.: Sea Ice Roughness Overlooked as a Key Source of Uncertainty in CryoSat-2 Ice
570   Freeboard Retrievals, Journal of Geophysical Research: Oceans, 125, e2019JC015 820, https://doi.org/10.1029/2019JC015820, 2020.

Larue, F., Picard, G., Aublanc, J., Arnaud, L., Robledano-Perez, A., LE Meur, E., Favier, V., Jourdain, B., Savarino, J., and Thibaut, P.:
       Radar Altimeter Waveform Simulations in Antarctica with the Snow Microwave Radiative Transfer Model (SMRT), Remote Sensing of
       Environment, 263, 112 534, https://doi.org/10.1016/j.rse.2021.112534, 2021.

Lawrence, I. R., Tsamados, M. C., Stroeve, J. C., Armitage, T. W. K., and Ridout, A. L.: Estimating Snow Depth over Arctic Sea Ice from
575   Calibrated Dual-Frequency Radar Freeboards, The Cryosphere, 12, 3551–3564, https://doi.org/10.5194/tc-12-3551-2018, 2018.

Laxon, S. W., Giles, K. A., Ridout, A. L., Wingham, D. J., Willatt, R., Cullen, R., Kwok, R., Schweiger, A., Zhang, J., Haas, C., Hendricks,
       S., Krishfield, R., Kurtz, N., Farrell, S., and Davidson, M.: CryoSat-2 Estimates of Arctic Sea Ice Thickness and Volume: CRYOSAT-2
       SEA ICE THICKNESS AND VOLUME, Geophysical Research Letters, 40, 732–737, https://doi.org/10.1002/grl.50193, 2013.

Löwe, H. and van Herwijnen, A.: A Poisson Shot Noise Model for Micro-Penetration of Snow, Cold Regions Science and Technology, 70,
580   62–70, https://doi.org/10.1016/j.coldregions.2011.09.001, 2012.

Meloche, J., Royer, A., Langlois, A., Rutter, N., and Sasseville, V.: Improvement of Microwave Emissivity Parameterization of Frozen Arctic Soils Using Roughness Measurements Derived from Photogrammetry, International Journal of Digital Earth, 14, 1380–1396, https://doi.org/10.1080/17538947.2020.1836049, 2021.

Montpetit, B., King, J., Meloche, J., Derksen, C., Siqueira, P., Adam, J. M., Toose, P., Brady, M., Wendleder, A., Vionnet, V., and Leroux,
N. R.: Retrieval of Airborne Ku-Band SAR Using Forward Radiative Transfer Modeling to Estimate Snow Water Equivalent: The Trail Valley Creek 2018/19 Snow Experiment, https://doi.org/10.5194/egusphere-2024-651, 2024.

Murfitt, J., Duguay, C. R., Picard, G., and Gunn, G. E.: Investigating the Effect of Lake Ice Properties on Multifrequency Backscatter Using the Snow Microwave Radiative Transfer Model, IEEE Transactions on Geoscience and Remote Sensing, 60, 1–23, https://doi.org/10.1109/TGRS.2022.3197109, 2022.

Murfitt, J., Duguay, C., Picard, G., and Gunn, G.: Forward Modelling of Synthetic Aperture Radar Backscatter from Lake Ice over Canadian Subarctic Lakes, Remote Sensing of Environment, 286, 113 424, https://doi.org/10.1016/j.rse.2022.113424, 2023.

Nandan, V., Geldsetzer, T., Yackel, J., Mahmud, M., Scharien, R., Howell, S., King, J., Ricker, R., and Else, B.: Effect of Snow Salinity on CryoSat-2 Arctic First-Year Sea Ice Freeboard Measurements: Sea Ice Brine-Snow Effect on CryoSat-2, Geophysical Research Letters, 44, 10,419–10,426, https://doi.org/10.1002/2017GL074506, 2017.

Nandan, V., Scharien, R. K., Geldsetzer, T., Kwok, R., Yackel, J. J., Mahmud, M. S., Rosel, A., Tonboe, R., Granskog, M., Willatt, R., Stroeve,
J., Nomura, D., and Frey, M.: Snow Property Controls on Modeled Ku-Band Altimeter Estimates of First-Year Sea Ice Thickness: Case Studies From the Canadian and Norwegian Arctic, IEEE Journal of Selected Topics in Applied Earth Observations and Remote Sensing, 13, 1082–1096, https://doi.org/10.1109/JSTARS.2020.2966432, 2020.

Nicolaus, M., Perovich, D. K., Spreen, G., Granskog, M. A., Von Albedyll, L., Angelopoulos, M., Anhaus, P., Arndt, S., Belter, H. J., Bessonov, V., Birnbaum, G., Brauchle, J., Calmer, R., Cardellach, E., Cheng, B., Clemens-Sewall, D., Dadic, R., Damm, E., De Boer, G., Demir, O., Dethloff, K., Divine, D. V., Fong, A. A., Fons, S., Frey, M. M., Fuchs, N., Gabarró, C., Gerland, S., Goessling, H. F., Gradinger, R., Haapala, J., Haas, C., Hamilton, J., Hannula, H.-R., Hendricks, S., Herber, A., Heuzé, C., Hoppmann, M., Høyland, K. V., Huntemann, M., Hutchings, J. K., Hwang, B., Itkin, P., Jacobi, H.-W., Jaggi, M., Jutila, A., Kaleschke, L., Katlein, C., Kolabutin, N., Krampe, D., Kristensen, S. S., Krumpen, T., Kurtz, N., Lampert, A., Lange, B. A., Lei, R., Light, B., Linhardt, F., Liston, G. E., Loose, B., Macfarlane, A. R., Mahmud, M., Matero, I. O., Maus, S., Morgenstern, A., Naderpour, R., Nandan, V., Niubom, A., Oggier, M., Oppelt, N., Pätzold, F., Perron, C., Petrovsky, T., Pirazzini, R., Polashenski, C., Rabe, B., Raphael, I. A., Regnery, J., Rex, M., Ricker, R., Riemann-Campe, K., Rinke, A., Rohde, J., Salganik, E., Scharien, R. K., Schiller, M., Schneebeli, M., Semmling, M., Shimanchuk, E., Shupe, M. D., Smith, M. M., Smolyanitsky, V., Sokolov, V., Stanton, T., Stroeve, J., Thielke, L., Timofeeva, A., Tonboe, R. T., Tavri, A., Tsamados, M., Wagner, D. N., Watkins, D., Webster, M., and Wendisch, M.: Overview of the MOSAiC Expedition: Snow and Sea Ice, Elementa: Science of the Anthropocene, 10, 000 046, https://doi.org/10.1525/elementa.2021.000046, 2022.

Picard, G., Sandells, M., and Löwe, H.: SMRT: An Active–Passive Microwave Radiative Transfer Model for Snow with Multiple Microstructure and Scattering Formulations (v1.0), Geoscientific Model Development, 11, 2763–2788, https://doi.org/10.5194/gmd-11-2763-2018, 2018.

Picard, G., Löwe, H., Domine, F., Arnaud, L., Larue, F., Favier, V., Le Meur, E., Lefebvre, E., Savarino, J., and Royer, A.: The Microwave Snow Grain Size: A New Concept to Predict Satellite Observations Over Snow-Covered Regions, AGU Advances, 3, https://doi.org/10.1029/2021AV000630, 2022.

Quartly, G. D., Rinne, E., Passaro, M., Andersen, O. B., Dinardo, S., Fleury, S., Guillot, A., Hendricks, S., Kurekin, A. A., Müller, F. L., Ricker, R., Skourup, H., and Tsamados, M.: Retrieving Sea Level and Freeboard in the Arctic: A Review of Current Radar Altimetry Methodologies and Future Perspectives, Remote Sensing, 11, 881, https://doi.org/10.3390/rs11070881, 2019.

620 Richter-Menge, J., Overland, J. E., Mathis, J. T., and Osborne, E.: Arctic Report Card 2017, 2017.

Ricker, R., Hendricks, S., Helm, V., Skourup, H., and Davidson, M.: Sensitivity of CryoSat-2 Arctic Sea-Ice Freeboard and Thickness on Radar-Waveform Interpretation, The Cryosphere, 8, 1607–1622, https://doi.org/10.5194/tc-8-1607-2014, 2014.

Ricker, R., Hendricks, S., and Beckers, J.: The Impact of Geophysical Corrections on Sea-Ice Freeboard Retrieved from Satellite Altimetry, Remote Sensing, 8, 317, https://doi.org/10.3390/rs8040317, 2016.

625 Sandells, M., Lowe, H., Picard, G., Dumont, M., Essery, R., Floury, N., Kontu, A., Lemmetyinen, J., Maslanka, W., Morin, S., Wiesmann, A., and Matzler, C.: X-Ray Tomography-Based Microstructure Representation in the Snow Microwave Radiative Transfer Model, IEEE Transactions on Geoscience and Remote Sensing, 60, 1–15, https://doi.org/10.1109/TGRS.2021.3086412, 2022.

Serreze, M. C. and Barry, R. G.: Processes and Impacts of Arctic Amplification: A Research Synthesis, Global and Planetary Change, 77, 85–96, https://doi.org/10.1016/j.gloplacha.2011.03.004, 2011.

630 Soriot, C., Picard, G., Prigent, C., Frappart, F., and Domine, F.: Year-Round Sea Ice and Snow Characterization from Combined Passive and Active Microwave Observations and Radiative Transfer Modeling, Remote Sensing of Environment, 278, 113 061, https://doi.org/10.1016/j.rse.2022.113061, 2022.

Tsang, L., Pan, J., Liang, D., Li, Z., Cline, D. W., and Tan, Y.: Modeling Active Microwave Remote Sensing of Snow Using Dense Media Radiative Transfer (DMRT) Theory With Multiple-Scattering Effects, IEEE Transactions on Geoscience and Remote Sensing, 45, 990–
635 1004, https://doi.org/10.1109/TGRS.2006.888854, 2007.

Tsang, L., Durand, M., Derksen, C., Barros, A. P., Kang, D.-H., Lievens, H., Marshall, H.-P., Zhu, J., Johnson, J., King, J., Lemmetyinen, J., Sandells, M., Rutter, N., Siqueira, P., Nolin, A., Osmanoglu, B., Vuyovich, C., Kim, E., Taylor, D., Merkouriadi, I., Brucker, L., Navari, M., Dumont, M., Kelly, R., Kim, R. S., Liao, T.-H., Borah, F., and Xu, X.: Review Article: Global Monitoring of Snow Water Equivalent Using High-Frequency Radar Remote Sensing, The Cryosphere, 16, 3531–3573, https://doi.org/10.5194/tc-16-3531-2022, 2022.

640 Vargel, C., Royer, A., St-Jean-Rondeau, O., Picard, G., Roy, A., Sasseville, V., and Langlois, A.: Arctic and Subarctic Snow Microstructure Analysis for Microwave Brightness Temperature Simulations, Remote Sensing of Environment, 242, 111 754, https://doi.org/10.1016/j.rse.2020.111754, 2020.

Willatt, R., Stroeve, J. C., Nandan, V., Newman, T., Mallett, R., Hendricks, S., Ricker, R., Mead, J., Itkin, P., Tonboe, R., Wagner, D. N., Spreen, G., Liston, G., Schneebeli, M., Krampe, D., Tsamados, M., Demir, O., Wilkinson, J., Jaggi, M., Zhou, L., Huntemann, M.,
645 Raphael, I. A., Jutila, A., and Oggier, M.: Retrieval of Snow Depth on Arctic Sea Ice From Surface-Based, Polarimetric, Dual-Frequency Radar Altimetry, Geophysical Research Letters, 50, e2023GL104 461, https://doi.org/10.1029/2023GL104461, 2023.

Wingham, D., Phalippou, L., Mavrocordatos, C., and Wallis, D.: The Mean Echo and Echo Cross Product from a Beamforming Interferometric Altimeter and Their Application to Elevation Measurement, IEEE Transactions on Geoscience and Remote Sensing, 42, 2305–2323, https://doi.org/10.1109/TGRS.2004.834352, 2004.